2D MULTI-PARAMETER VISCOELASTIC SHALLOW-SEISMIC FULL WAVEFORM INVERSION: RECONSTRUCTION TESTS AND FIRST FIELD-DATA APPLICATION

L. Gao, Y. Pan, and T. Bohlen

email: *lingli.gao@kit.edu*

keywords: *viscoelastic FWI, shallow seismic, multi parameters*

ABSTRACT

Full-waveform inversion (FWI) of shallow-seismic data is an attractive way to reconstruct multi-parameter models of the near surface with high resolution. In recent applications of shallow-seismic FWI, the effects of attenuation have been ignored to simplify the inversion. In this paper, we present the first synthetic reconstruction test of multi-parameter viscoelastic shallow-seismic FWI to reconstruct seismic velocities, density, and quality-factors on spatially correlated and uncorrelated models. The synthetic reconstructions tests reveal that simply ignoring the viscous effect will deteriorate the reconstruction of velocity and density models. Therefore, attenuation must be considered for reliable estimation of near-surface velocity models.

The multi-parameter viscoelastic FWI is also applied to shallow-seismic field data acquired in Rheinstetten, Germany. The main geological target, a refilled trench, is nicely delineated as a low-velocity anomaly in both reconstructed P- and S-wave velocity models. As a comparison, elastic FWI in which attenuation is considered as a passive modelling parameter leads to artefacts in the reconstructed S-wave and P-wave velocity models. A good agreement between reconstructed velocity models and a time-migrated GPR profile indicates a fairly high reliability of our inversion results.

INTRODUCTION

The reconstruction of near-surface models by using shallow-seismic wavefields plays an important role in geophysical and geotechnical site investigation. Shallow-seismic wavefields are dominated by surface waves, which makes the utilizing of surface waves an attractive way to reconstruct near-surface models. The inversion of surface waves is getting increasingly popular due to their high sensitivity to the S-wave velocity (Socco et al., 2010), which is an important lithological and geotechnical parameter to characterize the composition and stability of sediments.

Most of the current surface-wave methods are based on the extraction and the inversion of surface-wave dispersion curves (Xia et al., 1999). The dispersion-based surface-wave methods, however, fail when strong lateral heterogeneity exists, which is regarded as one of their limitations (Pan et al., 2019). Different approaches are proposed to account for lateral heterogeneity, such as laterally constrained inversion (Socco et al., 2009), cross-correlation analysis of multichannel data (Hayashi and Suzuki, 2004; Ikeda et al., 2013), and spatial windowing (Bohlen et al., 2004; Bergamo et al., 2012). Another limitation that current surface-wave methods face is the uncertainty in the correct estimation and identification of multi-modal dispersion curves (Boaga et al., 2013; Gao et al., 2014, 2016). Full waveform inversion (FWI) is attractive because it has the ability to produce high-resolution parameter models for complex geologic structures. FWI was first introduced by Tarantola (1984) and Mora (1987) in time domain with gradient-based inversion and has been proven as a powerful tool to reconstruct near-surface models by fitting the observed waveform directly (Romdhane et al., 2011; Tran et al., 2013; Groos et al., 2014, 2017; Pan et al., 2016, 2018; Mirzanejad and

Tran, 2019).

Besides the velocity model, the quality-factor (Q) model is also of fundamental interest, especially in groundwater, engineering, and environmental studies (Xia et al., 2002). Viscous effect mainly influences the amplitude of the seismic wave, and would also influence the phase of the seismic wave when strong attenuation (i.e., low Q value) exists (Groos et al., 2014). Several methods have been proposed to estimate Q from the attenuation coefficients of surface waves (Xia et al., 2002, 2012; Misbah and Strobbia, 2014; Gao et al., 2018). However, those methods are limited to a 1D earth model assumption. Viscous effects have been studied in the frequency domain visco-acoustic FWI (Virieux and Operto, 2009), in which Vp and Q can be inverted recursively or simultaneously (Kamei and Pratt, 2013; Malinowski et al., 2011). Brossier (2011) showed the potential of multi-parameter visco-elastic FWI by using a frequency-domain synthetic example. Bai et al. (2017) showed the reconstruction of attenuation in anisotropic viscoelastic media. Trinh et al. (2018) presented an efficient way to perform 3D elastic and viscoelastic FWI by using a spectral-element method. Besides the successful applications of FWI in exploration seismic that are focusing on the utilizing of body waves, there are few studies that are focusing on the reconstructing Q model of shallow subsurface. Groos et al. (2014) and Mirzanejad and Tran (2019) showed that the effects of anelastic damping must be considered in the shallow-seismic FWI for better reconstruction of high-resolution S-wave velocity model. A passive-viscoelastic FWI approach in which a fixed prior estimated Q model is used in the forward solver to compensate for the viscous effect.

Solving viscoelastic wave equation in time domain usually requires additional memory equations (Carcione et al., 1988; Robertsson et al., 1994; Bohlen, 2002). Since the viscoelastic wave equation is not self-adjoint, it is difficult to calculate the gradient by using the adjoint state method with the same numerical solver (Plessix, 2006). Different strategies have been proposed to solve this problem in viscoelastic FWI (Yang et al., 2016; Fabien-Ouellet et al., 2017), whose adjoint state equations are different from the forward equations. These approaches are equivalent to the pioneering works of Tarantola (1988) and Charara et al. (2000) on viscoelastic FWI in the displacement formulation.

In this paper, we study the performance of 2D multi-parameter viscoelastic FWI by accounting for viscoelasticity. General theories of the forward simulation and FWI workflow are given in the first section. Spatially correlated and uncorrelated models are performed to investigate the validity of multi-parameter viscoelastic FWI as well as to study the crosstalk between parameters. Viscoelastic and elastic FWI results are compared to investigate the necessity of including viscosity information. The crosstalk between Q_S and V_S is further investigated by using other two synthetic examples. We also apply viscoelastic FWI to a field shallow-seismic dataset acquired in Rheinstetten, Germany. For comparison, we also apply elastic FWI to the same field data. We evaluate the velocity models estimated by viscoelastic FWI by comparing them to a migrated GPR profile.

THEORY

Forward modelling

We adopt a velocity-stress formulation of the viscoelastic wave equation, in which the viscoelastic effects are modelled by generalized standard linear solid (GSLS) as

$$\frac{\partial \sigma_{ij}}{\partial t} = \frac{\partial v_k}{\partial x_k}\left[\frac{M\left(1+\tau_P\right)}{1+\alpha\tau_P} - \frac{2\mu\left(1+\tau_S\right)}{1+\alpha\tau_S}\right]\delta_{ij} + \left(\frac{\partial v_i}{\partial x_j} + \frac{\partial v_j}{\partial x_i}\right)\left[\frac{\mu\left(1+\tau_S\right)}{1+\alpha\tau_S}\right] + \sum_{l=1}^{L} r_{ijl} + f_{\sigma_{ij}}, \quad (1)$$

$$\rho\frac{\partial v_i}{\partial t} = \frac{\partial \sigma_{ij}}{\partial x_j} + f_{v_i}, \quad (2)$$

$$\frac{\partial r_{ij}}{\partial t} = -\frac{1}{\tau_{\sigma l}}\left[\frac{\partial v_k}{\partial x_k}\left(\frac{M\tau_P}{1+\alpha\tau_P} - \frac{2\mu\tau_S}{1+\alpha\tau_S}\right)\delta_{ij} + \left(\frac{\partial v_i}{\partial x_j} + \frac{\partial v_j}{\partial x_i}\right)\frac{\mu\tau_S}{1+\alpha\tau_S} + r_{ijl}\right], \quad (3)$$

where Einstein summation convention is used here over spatial indices i, j and k; σ_{ij} is the ijth component of the stress tensor; v_i is the velocity tensor; r_{ij} is the memory variable corresponding to the stress tensor σ_{ij}; f is the external force; $\tau_{\sigma l}$ is the stress relaxation time of the lth Maxwell body; L is the total number of Maxwell bodies; τ_S and τ_P are attenuation levels of S wave and P wave, respectively; M and μ are

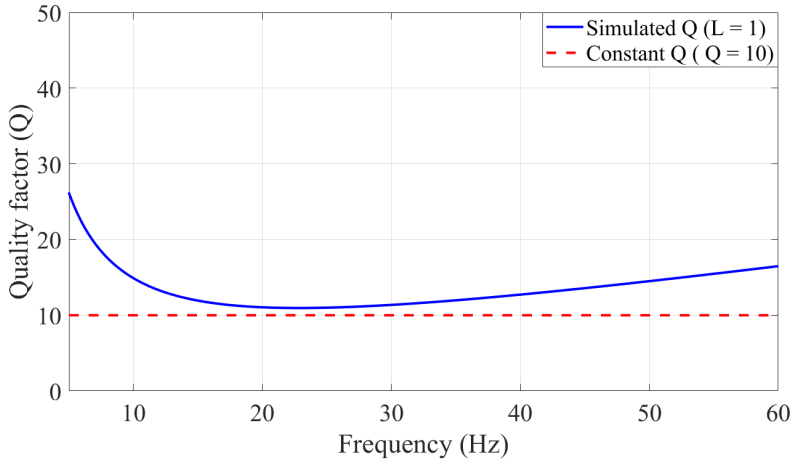

Figure 1: Comparison of a constant Q value and the Q values simulated by using one relaxation mechanism.

the P-wave and S-wave modulus, respectively; α is used to define the propagation velocities at a reference frequency.

The attenuation property of the materials is defined as the ratio between the real and imaginary parts of the complex modulus (O'Connell and Budiansky, 1978), and the quality factor can be described as

$$Q = \frac{1 + \sum_{l=1}^{L} \frac{\omega^2 \tau_{\sigma l}^2}{1+\omega^2 \tau_{\sigma l}^2} \tau}{\sum_{l=1}^{L} \frac{\omega \tau_{\sigma l}}{1+\omega^2 \tau_{\sigma l}^2} \tau}, \tag{4}$$

where the $\tau_{\sigma l}$ controls the frequency peak locations of the lth Maxwell bodies and is taken as a spatially constant variable before the simulation. The attenuation level τ controls the magnitude of the quality factor (i.e., $\tau = \frac{2}{Q}$).

A desired constant Q in a limited frequency range can be approximated with different Maxwell bodies (Blanch et al., 1995). Figure 1 shows the shape of a desired and the simulated Q values by using only one Maxwell body (Bohlen, 2002). The constant Q of 10 is well approximated in the frequency band between 10 Hz and 60 Hz, which covers most of the frequency range of shallow-seismic data. Therefore, we only use a single relaxation mechanism in this paper.

Full waveform inversion

FWI is an iterative optimization technique that seeks to estimate an optimal subsurface model $\mathbf{m}$ (V_S, V_P, ρ, τ_S, τ_P) by minimizing the difference between the synthetic and observed seismic waveforms. In this paper, we use the least-squares l_2-error between the non-normalized synthetic and observed particle-velocity waveforms as the objective function:

$$\Psi(\mathbf{m}) = \frac{1}{2} ||\mathbf{d}^{syn}(\mathbf{m}) - \mathbf{d}^{obs}||^2, \tag{5}$$

where $\mathbf{d}^{syn}(\mathbf{m})$ and $\mathbf{d}^{obs}$ are the synthetic and observed particle-velocity waveforms, respectively.

Adjoint state method provides an efficient way to calculate the gradient of misfit function by cross-correlating the forward (state variables) and backward (adjoint state variables) wavefields. The backward wavefields can be calculated by solving the adjoint state equations (Fabien-Ouellet et al., 2017), which can

be written as

$$\begin{aligned}\frac{\partial \overleftarrow{\sigma_{ij}}}{\partial t'} =& -\frac{\partial \overleftarrow{v_k}}{\partial x_k}\left[\frac{M\left(1+\tau_P\right)}{1+\alpha\tau_P}-\frac{2\mu\left(1+\tau_S\right)}{1+\alpha\tau_S}\right]\delta_{ij}-\left(\frac{\partial \overleftarrow{v_i}}{\partial x_j}+\frac{\partial \overleftarrow{v_j}}{\partial x_i}\right)\frac{\mu\left(1+\tau_S\right)}{1+\alpha\tau_S}-\sum_{l=1}^{L}\overleftarrow{r_{ijl}} \\ &+\left[\frac{M\left(1+\tau_P\right)}{1+\alpha\tau_P}-\frac{2\mu\left(1+\tau_S\right)}{1+\alpha\tau_S}\right]\delta_{ij}\frac{\partial\Psi}{\partial\sigma_{kk}}+\mu\frac{1+\tau_S}{1+\alpha\tau_S}\left(1+\delta_{ij}\right)\frac{\partial\Psi}{\partial\sigma_{ij}}\end{aligned} \tag{6}$$

$$\rho\frac{\partial \overleftarrow{v_i}}{\partial t'} = -\frac{\partial \overleftarrow{\sigma_{ij}}}{\partial x_j}+\frac{\partial\Psi}{\partial v_i} \tag{7}$$

$$\frac{\partial \overleftarrow{r_{ij}}}{\partial t'} = -\frac{1}{\tau_{\sigma l}}\left[\frac{\partial \overleftarrow{v_k}}{\partial x_k}\left(\frac{M\tau_P}{1+\alpha\tau_P}-\frac{2\mu\tau_S}{1+\alpha\tau_S}\right)\delta_{ij}+\left(\frac{\partial \overleftarrow{v_i}}{\partial x_j}+\frac{\partial \overleftarrow{v_j}}{\partial x_i}\right)\frac{\mu\tau_S}{1+\alpha\tau_S}+\overleftarrow{r_{ijl}}\right] \tag{8}$$

with $t' = T - t$.

Compared to the forward modelling equations (equations 1-3), the adjoint state equations (equations 6-8) only differ in the source terms and the sign before the spatial derivatives; therefore, they can be solved with the 'same' forward modelling code. Misfit gradients for parameters S-wave modulus, P-wave modulus, ρ, τ_S, τ_P are given in Fabien-Ouellet et al. (2017). Then the gradients in term of V_S, V_P, ρ, τ_S, τ_P can be calculated by applying the chain rule on the Fréchet kernels.

We use a finite-difference method to solve the wave equations and its adjoint equations (Bohlen, 2002). The model parameters are updated iteratively via

$$\mathbf{m}_{k+1} = \mathbf{m}_k + \lambda\delta\mathbf{m}_{k+1}, \tag{9}$$

where the step length λ is calculated by a combination of line search and parabolic fitting. The model update direction $\delta\mathbf{m}_{k+1}$ is calculated via a preconditioned conjugate gradient algorithm and parameter scaling (Yang et al., 2018). A multi-scale inversion strategy is used to avoid cycle skipping (Bunks et al., 1995).

SYNTHETIC EXAMPLES

In this section, we perform synthetic tests to explore the properties of 2D multi-parameter viscoelastic FWI. We firstly perform two multi-parameter (five-parameters) examples by using a spatially uncorrelated and a spatially correlated model, respectively. Results of viscoelastic and elastic FWIs are also compared. Then we further investigate the crosstalk between coupled parameters V_S and τ_S by comparing multi-parameter (two-parameters) viscoelastic and mono-parameter elastic FWI results.

Multi-parameter examples

We build a true model that consists of a depth-dependent 1-D background model. A triangular low-value anomaly is superimposed on each parameter model at different positions (Fig. 2). Each triangular anomaly is 8 m wide and 4 m deep. The contrast between the anomaly and the background model in the Q models (e.g., $Q_s = 10$ compared to $Q_s \approx 80$) is stronger than the contrasts in the velocity and the density models (e.g., $V_S = 120$ m/s compared to $V_S \approx 180$ m/s, $\rho = 1850$ kg/m^3 compared to $\rho \approx 2100$ kg/m^3). We use a total of 10 shots with a source spacing of 10 m, starting from $X = 20$ m to $X = 110$ m. The vertical-force source is generated by a delayed Ricker wavelet with a central frequency of 30 Hz. A total of 91 receivers (recording both vertical and horizontal components) are distributed along the free surface with an equidistant spacing of 1 m, starting from $X = 20$ m to $X = 110$ m. The 1-D background models are used as the initial models, and the true source wavelet is used during the inversion. We perform a multi-parameter viscoelastic FWI on the synthetic data in which all five parameters are updated simultaneously during the inversion. A high-cut frequency filter of 25, 35, 45, and 60 Hz is used progressively in the multi-scale strategy. The reconstructed multi-parameter models show a nice agreement with the true models (first and second columns in Fig.2), especially for the velocity parameters V_S and V_P. On the contrary, the viscosity models are only roughly reconstructed. In the inverted τ_P model the triangular anomaly cannot be identified. This reconstruction test shows that viscoelastic FWI is more sensitive to the velocities than

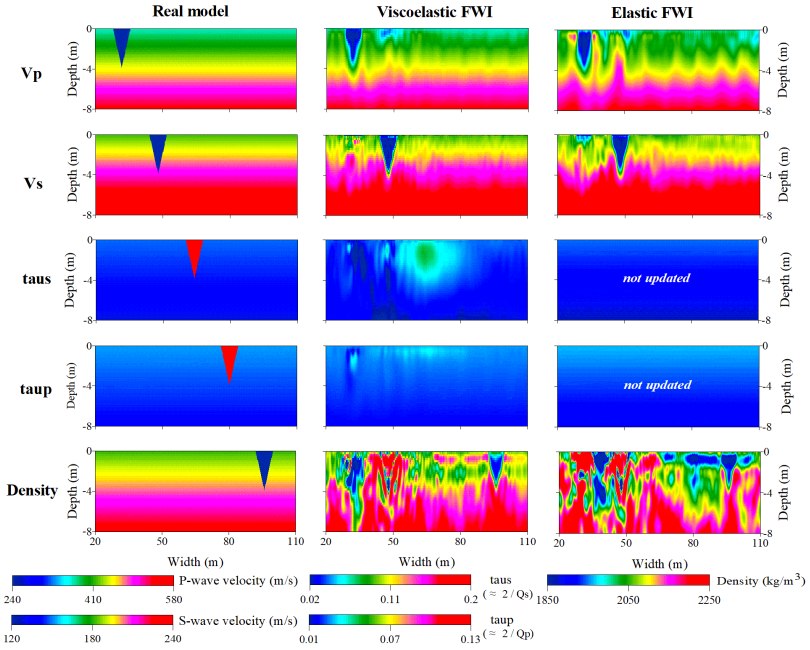

Figure 2: Multi-parameter synthetic example on a spatially uncorrelated model. Three columns represent the true models, viscoelastic FWI results, and elastic FWI results, respectively. The 1-D background models are used as the initial models for the inversion.

the quality factors. Although the triangular anomaly can be easily identified in the reconstructed density model, the density model suffers strong crosstalks from the velocity models at the position where the V_S and V_P anomalies locate. Furthermore, the density model is also contaminated by strong fluctuations in the shallow part (depth < 4 m), indicating a moderate sensitivity of viscoelastic FWI with respect to density in the vicinity of the free surface.

The reconstructed models show the interactions between the five parameters. V_S has strong crosstalk to all the other parameters except for τ_P, and only weakly suffers crosstalk from V_P. V_P has strong crosstalk to τ_P and density and suffers crosstalk mainly from V_S. Due to relatively low sensitivity of surface waves with respect to τ_S and τ_P, they mainly suffer crosstalk from the corresponding coupled velocity (i.e., V_S and V_P, respectively), and their footprints on the other parameters can be hardly identified. Similarly, the density model suffers strong crosstalk from both V_S and V_P but only weakly pass crosstalk to the other parameters. Overall, strong crosstalk mainly exists between V_S and V_P, from velocity to viscosity models between coupled pair (i.e., V_S to τ_S, V_P to τ_P), and from velocity to density models.

In order to study the relative importance of attenuation, we perform an elastic FWI with fixed Q model on the same dataset. Though named as elastic, the 1D linear-gradient τ models are used in a viscoelastic forward solver but not updated during the inversion (it is sometimes also called 'viscoelastic', 'pseudo-viscoelastic', or 'passive-viscoelastic' FWI since a viscoelastic forward solver is used). Due to the high sensitivity of Rayleigh wave with respect to V_S, the final V_S model is recovered quite robustly. The V_P model reconstructed by elastic FWI (third column in Fig.2) contains vertical-stripes artefacts (wavefront-like artefacts, since the Rayleigh waves mainly propagate horizontally with a vertical wavefront), which do not exist in the viscoelastic FWI result. The triangular shape of V_P anomaly is less accurately delineated in the elastic FWI result compared to the viscoelastic result. The crosstalk between V_P and V_S becomes stronger in the elastic FWI results since it has fewer parameters to explain the data. The density model contains strong artefacts in the shallow part (depth < 4 m) and is worse than the density model reconstructed by viscoelastic FWI. Overall, the reconstruction of V_S model is quite robust regardless of whether viscoelastic or elastic FWI is used, and viscoelastic FWI results contain weaker artefacts compared to the elastic FWI results. Worse results would be obtained if we fully ignore attenuation effects and just perform purely elastic FWI on the data (Groos et al., 2014).

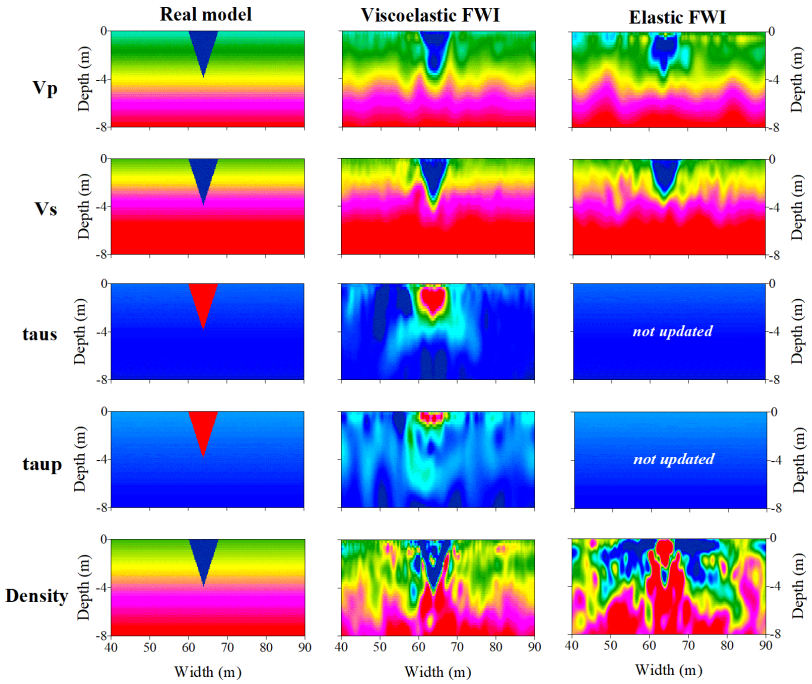

Figure 3: Multi-parameter synthetic example on a spatially correlated model. Three columns represent the true models, viscoelastic FWI results, and elastic FWI results, respectively. The 1-D background models are used as the initial models for the inversion. All the colour scales are identical to Fig.2.

In the second experiment, we shift all the anomalies in different model parameters to the same position (first row in Fig.3). This spatially correlated model is generally more realistic compared to the previous one since all the physical-parameter anomalies usually belong to the same geological target and, thus, are spatially correlated. The same acquisition geometry, initial models, and inversion parameters as in the first example are used. Similarly, we also perform both viscoelastic and elastic FWIs on the same dataset for comparison.

All five parameter models are nicely reconstructed in the viscoelastic FWI results (second column in Fig.3). The triangular shape of the anomaly is better delineated in the V_S model compared to the V_P model. We can see the location of the anomaly in both τ_S and τ_P models with a more accurate estimation of the values compared to the spatially-uncorrelated example. Although the density model also delineates the existence of the low-value triangular anomaly, it suffers from much stronger artefacts compared to the other parameter models.

The elastic FWI results with fixed Q models also nicely resolves the location and the velocity structure of the anomaly (third column in Fig.3). The triangular shapes of both V_P and V_S anomalies, however, are worse delineated compared to the viscoelastic FWI results. The reconstructed density model shows basically a wrong result in which a high-density anomaly instead of the low-density anomaly is reconstructed.

Overall, both two synthetic experiments show that the reconstruction of V_S is quite robust regardless of whether viscoelastic or elastic FWI is adopted. The viscoelastic FWI provides more accurate and comprehensive results compared to elastic FWI, especially for the reconstruction of V_P. The effect of attenuation is contaminated by the footprint from the velocity, while the velocity is relatively unaffected by the attenuation.

Crosstalk between coupled velocity and quality factor

We perform another two synthetic tests to investigate the crosstalk between coupled parameters: V_S and τ_S, because of the high sensitivity of Rayleigh wave with respect to V_S and Q_S (τ_S) compared to V_P and Q_P (τ_P) (Xia et al., 2002; Groos et al., 2017).

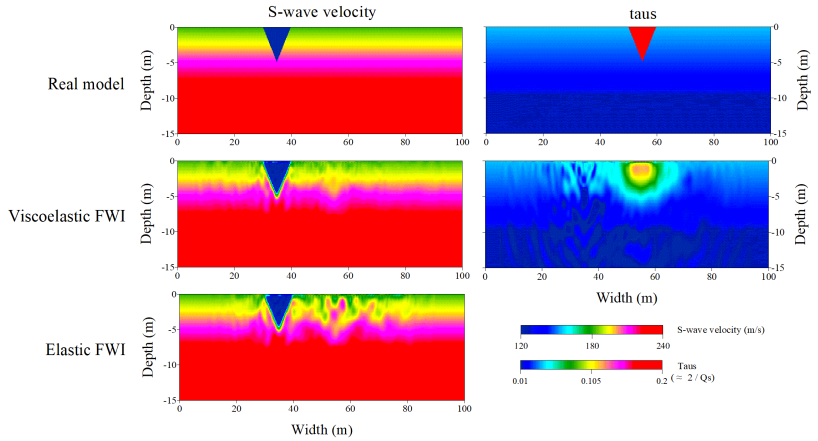

Figure 4: First two-parameter synthetic example on a spatially uncorrelated model. Left and right columns are the V_S and τ_S models, respectively. Three rows are the true models, two-parameter viscoelastic FWI results, and mono-parameter elastic FWI result, respectively.

We use the same 1D background models for velocities and quality factors, but only superimpose a low-V_S anomaly and a low-Q_s (high-τ_S) anomaly at different positions (first row, Fig. 4). We add a water table at 10 m depth, and the P-wave velocity below the water table is set as 1500 m/s. A homogeneous density model with a value of 2050 kg/m^3 is used. A total of 7 vertical-force source positions are placed with a spacing of 10 m from $X = 20$ m to $X = 80$ m. The sources are generated with a delayed Ricker wavelet of 30 Hz. A total of 61 two-component receivers are distributed along the free surface with an equidistant spacing of 1 m from the first to the last source positions. The 1-D background models are used as the initial models, and we only update V_S and τ_S models during the inversion.

In the spatially uncorrelated test, the reconstructed V_S model by viscoelastic FWI (second row in Fig.4) shows a nice agreement with the true model and is slightly affected by the τ_S anomaly. On the contrary, the τ_S model is only roughly reconstructed and the value of τ_S anomaly is underestimated. Besides, it is contaminated by the crosstalk from the V_S model with a footprint from the V_S anomaly. A poor reconstruction of the value of τ_S anomaly indicates that viscoelastic FWI is more sensitive with respect to V_S compared to τ_S.

For comparison, we perform an elastic FWI by adopting and keeping the background τ_S model during the inversion. The reconstructed V_S model (third row, Fig.4) clearly shows the location, shape and the value of the V_S anomaly. Relatively strong artefacts, however, appear in the vicinity of the τ_S anomaly position. Those unwanted artefacts arise during the inversion to produce similar effects as anelasticity. Obviously, the S-wave velocity model is much better reconstructed via viscoelastic FWI compared to elastic FWI.

Similarly, we perform a similar synthetic test on a spatially correlated model in which V_S and τ_S anomalies locate at the same location (first row in Fig. 5). Both V_S and τ_S models are successfully recovered by viscoelastic FWI. In the result of elastic FWI, however, strong artefacts and distortion appear in the surrounding area of the anomaly (third row, Fig. 5). These artefacts behave as vertical-stripped anomalies, which are parallel to the wavefront of Rayleigh-wave. The shape of the anomaly is much clearer delineated by viscoelastic FWI compared to the elastic FWI. Overall, these two examples again show that the multi-parameter viscoelastic FWI provides better result compared to the elastic FWI. If we neglect attenuation and do not invert for it, the heterogeneity of Q_S models can be projected into the reconstructed S-wave velocity model.

APPLICATION TO FIELD DATA

We apply the multi-parameter viscoelastic FWI strategy to a shallow seismic field dataset. The test site is located on a glider airfield in Rheinstetten, Germany. The shallow subsurface is composed of fluviatile sediments from the late Pleistocene. A refilled trench, namely "Ettlinger Linie" (EL), is approximately located in the middle of our survey line (Wittkamp et al., 2019). The seismic dataset is excited by vertical

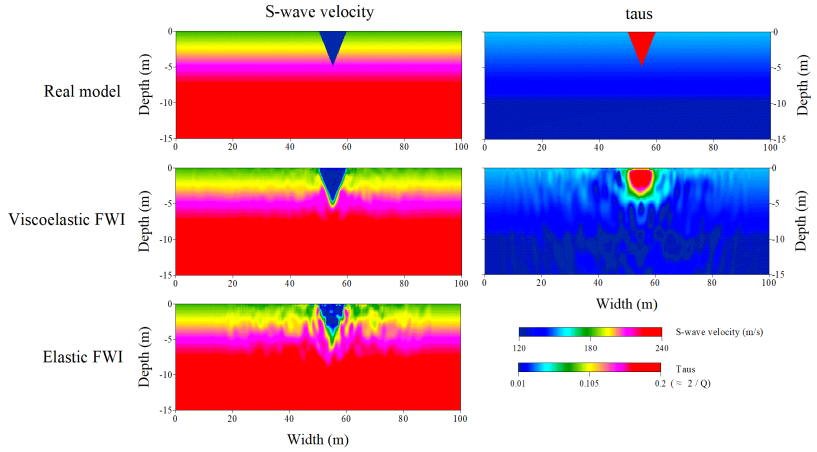

Figure 5: Second two-parameter synthetic example on a spatially correlated model. Left and right columns are the V_S and Q_s models, respectively. Three rows are the true models, two-parameter viscoelastic FWI results, and mono-parameter elastic FWI result, respectively.

hammer blows and recorded by 48 vertical geophones spaced every 1 m. A total of 12 shots with a 4-m spacing are used (asterisks in Fig. 6). The first source position is located between the first and second geophones. We perform a 3D-2D transformation (Forbriger et al., 2014) to the observed data and remove the bad traces before FWI.

We mainly use surface-wave methods to build the initial models for FWI to reduce the possibility of cycle skipping (1st column in Fig. 6). 1D V_S and Q_s models are estimated by the inversions of Rayleigh-wave dispersion curve and attenuation coefficients (Gao et al., 2018), respectively. The initial 1D V_P model is estimated by first-arrival traveltime inversion. For the initial Q_p model $Q_P = Q_S$ is assumed. A linear gradient model is used as the initial density model.

The multi-scale strategy starts with low-pass filtered data up to 10 Hz. The frequency content is progressively increased by 5 Hz until 60 Hz is reached. A minimum of three iterations is guaranteed in each scale, and the inversion moved to next scale when the relative decrease in the misfit value is less than 1%. Although we update τ models instead of Q models during the inversion, we show Q models in the final results due to their physical meaning.

The multi-parameter inversion results are shown in the 2nd column in Fig. 6. The inverted V_S model shows a triangular low-velocity anomaly in the central part of the spread, indicating the existence and the location of the EL. A similar low-velocity anomaly can also be identified in the final V_P model. The Q_s and Q_p models show relatively low Q values ($Q < 15$) in the shallow subsurface (top 2 m), and relatively higher Q values in the deeper part. It indicates that the attenuation in seismic waves is mainly caused by the shallow soil (weathering zone). The final ρ model doesn't provide geological information about the trench, which may be caused by the relatively low sensitivity of Rayleigh waves with respect to density. Overall, the inversion of the field data provides a relatively high resolution in the velocity models and a relatively low resolution in the Q and density models. Twelve inverted source time functions (Fig. 7) show high similarity among each other, indicating that estimated source time functions are fairly reliable. The synthetic waveforms fit the observed data fairly well (Fig. 8), which indicates a successful explanation of the observed wavefield by the final multi-parameter models.

In order to study the role of attenuation for the Rheinstetten study area, we also perform elastic FWI tests on the same data by using a fixed initial depth-dependent Q model and a homogeneous Q model during the inversion (third and fourth columns in Fig. 6), respectively. The inverted V_S and V_P models show a similar low-velocity anomaly. However, they are contaminated with vertical-striped artefacts, which is mainly caused by ignoring the heterogeneity in the Q models. Similar artefacts have also been observed in our synthetic reconstruction tests. The existence of the artefacts makes it difficult to identify the shape of the EL in the reconstructed P-wave velocity model.

In order to validate our final FWI model, we also compare our velocity models obtained by viscoelastic

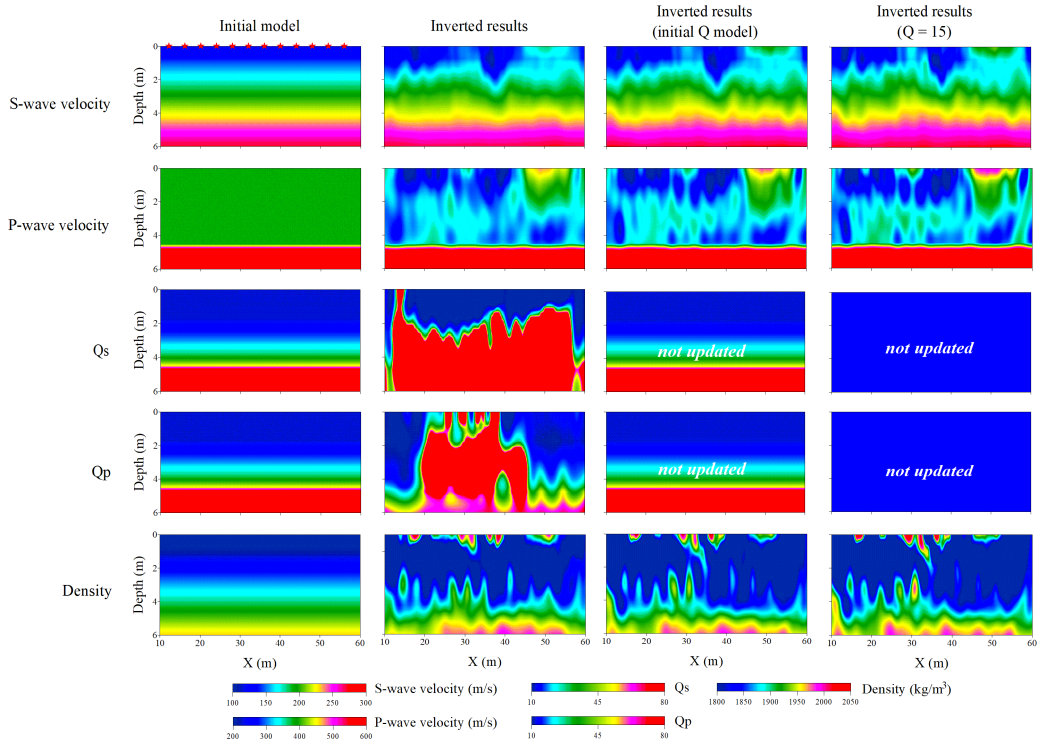

Figure 6: Comparison of reconstructed models (V_S, V_P, Q_s, Q_p, ρ) obtained from shallow-seismic FWI. The first colum represents the initial models. The second column shows the inversion results of multi-parameter viscoelastic FWI. The third and fourth columns show the inversion results obtained by multi-parameter elastic FWI without updating Q model. The fixed Q models for the third and fourth columns are the depth-dependent and homogeneous Q models, respectively.

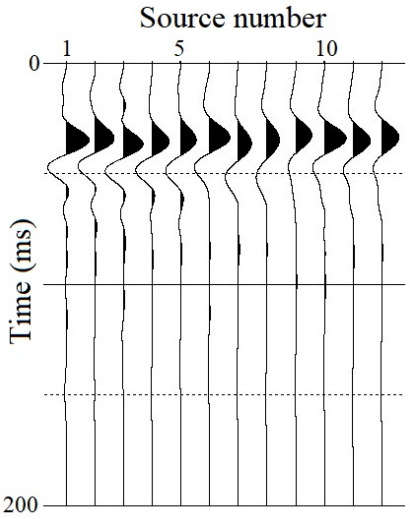

Figure 7: The estimated source time functions of the twelve shot gathers.

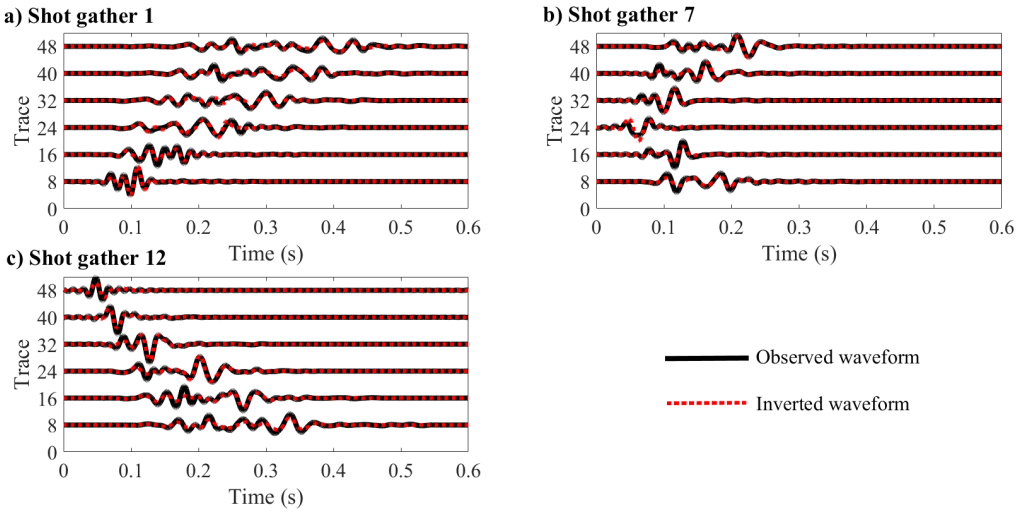

Figure 8: Comparison of vertical velocity seismograms in the first, seventh, and last shots. Thick black lines are the observed seismograms. Red dashed lines are the synthetic seismograms corresponding to the inversion results of multi-parameter viscoelastic FWI. The waveform in each trace is scaled by its offset.

FWI (2nd column in Figure 6) to a migrated GPR profile acquired along the same survey line (Fig. 9). The comparison with the GPR section shows a fairly good agreement with respect to the location and the shape of the EL. It verifies fairly high reliability of the final S- and P-wave velocity models estimated by the multi-parameter viscoelastic FWI.

DISCUSSIONS

In the present study, we show that a multi-parameter viscoelastic FWI can improve the accuracy of the estimated velocity models and is superior to the elastic FWI in which attenuation is considered as a passive modelling parameter only. In general, the resolution of the estimated quality-factor models is much poorer compared to the resolution of the velocity models. The adoption of an amplitude-based misfit function may improve the sensitivity to quality factor as well as the inversion result of Q models (Pan and Innanen, 2019). Only one relaxation mechanism has been used in this study to describe the frequency dependency of Q for the sake of computational cost. Since we only use single relaxation mechanism, the estimated Q values might be lower than their true values (Fig. 1). The importance of considering multiple relaxation mechanisms needs to be further investigated in the future.

Multi-parameter inversion including seismic velocities and quality factors of both P- and S-waves can provide more detailed information to improve the characterization of the shallow subsurface. However, the inversion results can be contaminated by crosstalk between the perturbations of different parameters, which decreases the reliability of the reconstructed models. In this paper, we use a preconditioned conjugate gradient algorithm to invert the data, which cannot reduce the parameter trade-off effects between coupled parameters appropriately. This is because that the cross-parameter information locates in the off-diagonal part of the Hessian matrix, while we only use an approximation of the diagonal of Hessian matrix for preconditioning. The neglecting of the off-diagonal part of Hessian does not pose a severe problem when the multi-parameter models are spatially correlated (e.g., Fig. 3). The utilizing of second-order optimization algorithm (Operto et al., 2013; Métivier et al., 2013) for reducing parameter trade-offs in the viscoelastic FWI of shallow-seismic data needs to be further investigated.

CONCLUSIONS

In this paper, 2D multi-parameter viscoelastic full-waveform inversion (FWI) is applied to shallow seismic data, presented for improving geotechnical site characterization. We tested the capability of the method to reconstruct reliable parameters on synthetic datasets with spatially correlated and uncorrelated models.

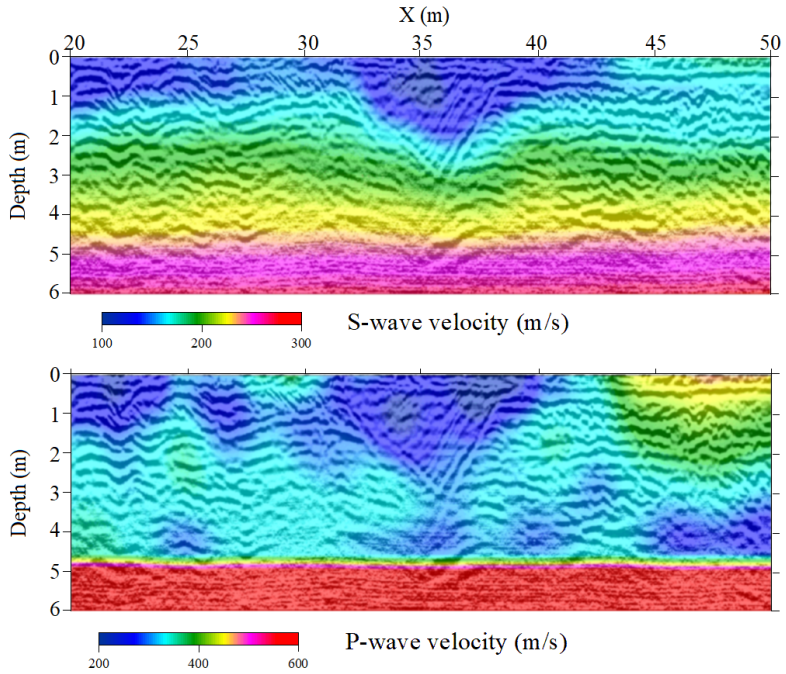

Figure 9: Comparison between the field-data inversion results and a GPR profile. The S-wave velocity and P-wave velocity models are overlying on the time-migrated image of the GPR measurement.

The synthetic results of spatially uncorrelated models showed that shallow-seismic data has the highest sensitivity with respect to V_S, then V_P, and relatively low sensitivity to density, Q_S and Q_P. They also showed that crosstalk mainly exists between velocity models (i.e., V_S and V_P) and coupled velocity-quality factor pairs (i.e., V_S and Q_S, V_P and Q_P). Crosstalk between coupled parameters V_S and τ_S was further investigated by another two synthetic examples in which strong crosstalk from V_S to τ_S is observed. If attenuation is not updated, artefacts in the estimated velocity models may be developed. All these synthetic examples showed that multi-parameter viscoelastic FWI could improve the accuracy of the inversion results compared to the elastic FWI.

We applied the multi-parameter viscoelastic FWI approach to a field shallow-seismic dataset acquired in Rheinstetten, Germany. The final V_S and V_P models revealed a sharp triangular low-velocity anomaly, which accurately delineates the location and the shape of a known refilled trench. We compared our viscoelastic FWI result to the results estimated by elastic FWI in which Q models were included but not updated during the inversion. Although the elastic results could also reveal the triangular low-velocity anomaly in the V_S models, they were contaminated by vertical-striped artefacts, which was mainly caused by the neglecting of heterogeneity in the Q models. A good agreement between our viscoelastic FWI result and a migrated GPR profile verified the accuracy of our estimated models and validity of the method. Mitigation of crosstalk between coupled parameters needs to be studied in the future.

ACKNOWLEDGMENTS

This work was funded by the Deutsche Forschungsgemeinschaft (DFG, German Research Foundation) Project-ID 258734477-SFB 1173.This work was kindly supported by the sponsors of the *Wave Inversion Technology (WIT) Consortium*, Karlsruhe, Germany.

REFERENCES

Bai, T., Tsvankin, I., and Wu, X. (2017). Waveform inversion for attenuation estimation in anisotropic media. *Geophysics*, 82(4):WA83–WA93.

Bergamo, P., Boiero, D., and Socco, L. V. (2012). Retrieving 2D structures from surface-wave data by means of space-varying spatial windowing. *Geophysics*, 77(4):EN39–EN51.

Blanch, J. O., Robertsson, J. O., and Symes, W. W. (1995). Modeling of a constant Q: Methodology and algorithm for an efficient and optimally inexpensive viscoelastic technique. *Geophysics*, 60(1):176–184.

Boaga, J., Cassiani, G., Strobbia, C. L., and Vignoli, G. (2013). Mode misidentification in Rayleigh waves: Ellipticity as a cause and a cure. *Geophysics*, 78(4):EN17–EN28.

Bohlen, T. (2002). Parallel 3-D viscoelastic finite difference seismic modelling. *Computers & Geosciences*, 28(8):887–899.

Bohlen, T., Kugler, S., Klein, G., and Theilen, F. (2004). 1.5D inversion of lateral variation of Scholte wave dispersion. *Geophysics*, 69(2):330–344.

Brossier, R. (2011). Two-dimensional frequency-domain visco-elastic full waveform inversion: Parallel algorithms, optimization and performance. *Computers & Geosciences*, 37(4):444–455.

Bunks, C., Saleck, F. M., Zaleski, S., and Chavent, G. (1995). Multiscale seismic waveform inversion. *Geophysics*, 60(5):1457–1473.

Carcione, J. M., Kosloff, D., and Kosloff, R. (1988). Wave propagation simulation in a linear viscoelastic medium. *Geophysical Journal International*, 95(3):597–611.

Charara, M., Barnes, C., and Tarantola, A. (2000). Full waveform inversion of seismic data for a viscoelastic medium. In *Methods and applications of inversion*, pages 68–81. Springer.

Fabien-Ouellet, G., Gloaguen, E., and Giroux, B. (2017). Time domain viscoelastic full waveform inversion. *Geophysical Journal International*, 209(3):1718–1734.

Forbriger, T., Groos, L., and Schäfer, M. (2014). Line-source simulation for shallow-seismic data. Part 1: Theoretical background. *Geophysical Journal International*, 198(3):1387–1404.

Gao, L., Pan, Y., Tian, G., and Xia, J. (2018). Estimating Q factor from multi-mode shallow-seismic surface waves. *Pure and Applied Geophysics*, 175(8):2609–2622.

Gao, L., Xia, J., and Pan, Y. (2014). Misidentification caused by leaky surface wave in high-frequency surface wave method. *Geophysical Journal International*, 199(3):1452–1462.

Gao, L., Xia, J., Pan, Y., and Xu, Y. (2016). Reason and condition for mode kissing in MASW method. *Pure and Applied Geophysics*, 173(5):1627–1638.

Groos, L., Schäfer, M., Forbriger, T., and Bohlen, T. (2014). The role of attenuation in 2D full-waveform inversion of shallow-seismic body and Rayleigh waves. *Geophysics*, 79(6):R247–R261.

Groos, L., Schäfer, M., Forbriger, T., and Bohlen, T. (2017). Application of a complete workflow for 2D elastic full-waveform inversion to recorded shallow-seismic Rayleigh waves. *Geophysics*, 82(2):R109–R117.

Hayashi, K. and Suzuki, H. (2004). CMP cross-correlation analysis of multi-channel surface-wave data. *Exploration Geophysics*, 35(0):7–13.

Ikeda, T., Tsuji, T., and Matsuoka, T. (2013). Window-controlled CMP crosscorrelation analysis for surface waves in laterally heterogeneous media. *Geophysics*, 78(6):EN95–EN105.

Kamei, R. and Pratt, R. (2013). Inversion strategies for visco-acoustic waveform inversion. *Geophysical Journal International*, 194(2):859–884.

Malinowski, M., Operto, S., and Ribodetti, A. (2011). High-resolution seismic attenuation imaging from wide-aperture onshore data by visco-acoustic frequency-domain full-waveform inversion. *Geophysical Journal International*, 186(3):1179–1204.

Métivier, L., Brossier, R., Virieux, J., and Operto, S. (2013). Full waveform inversion and the truncated newton method. *SIAM Journal on Scientific Computing*, 35(2):B401–B437.

Mirzanejad, M. and Tran, K. T. (2019). 3D viscoelastic full waveform inversion of seismic waves for geotechnical site investigation. *Soil Dynamics and Earthquake Engineering*, 122:67–78.

Misbah, A. S. and Strobbia, C. L. (2014). Joint estimation of modal attenuation and velocity from multi-channel surface wave data. *Geophysics*, 79(3):EN25–EN38.

Mora, P. (1987). Nonlinear two-dimensional elastic inversion of multioffset seismic data. *Geophysics*, 52(9):1211–1228.

O'Connell, R. and Budiansky, B. (1978). Measures of dissipation in viscoelastic media. *Geophysical Research Letters*, 5(1):5–8.

Operto, S., Gholami, Y., Prieux, V., Ribodetti, A., Brossier, R., Metivier, L., and Virieux, J. (2013). A guided tour of multiparameter full-waveform inversion with multicomponent data: From theory to practice. *The Leading Edge*, 32(9):1040–1054.

Pan, W. and Innanen, K. A. (2019). Amplitude-based misfit functions in viscoelastic full-waveform inversion applied to walk-away vertical seismic profile data. *Geophysics*, 84(5):1–66.

Pan, Y., Gao, L., and Bohlen, T. (2018). Time-domain full-waveform inversion of Rayleigh and Love waves in presence of free-surface topography. *Journal of Applied Geophysics*, 152:77 – 85.

Pan, Y., Gao, L., and Bohlen, T. (2019). High-resolution characterization of near-surface structures by surface-wave inversions: from dispersion curve to full waveform. *Surveys in Geophysics*, 40(2):167–195.

Pan, Y., Xia, J., Xu, Y., Gao, L., and Xu, Z. (2016). Love-wave waveform inversion for shallow shear-wave velocity using a conjugate gradient algorithm. *Geophysics*, 81(1):R1–R14.

Plessix, R. (2006). A review of the adjoint-state method for computing the gradient of a functional with geophysical applications. *Geophysical Journal International*, 167(2):495–503.

Robertsson, J. O., Blanch, J. O., and Symes, W. W. (1994). Viscoelastic finite-difference modeling. *Geophysics*, 59(9):1444–1456.

Romdhane, A., Grandjean, G., Brossier, R., Rejiba, F., Operto, S., and Virieux, J. (2011). Shallow-structure characterization by 2D elastic full waveform inversion. *Geophysics*, 76(3):R81–R93.

Socco, L., Boiero, D., Foti, S., and WisÃl'n, R. (2009). Laterally constrained inversion of ground roll from seismic reflection records. *Geophysics*, 74(6):G35–G45.

Socco, L., Foti, S., and Boiero, D. (2010). Surface wave analysis for building near surface velocity models: established approaches and new perspectives. *Geophysics*, 75(5):A83–A102.

Tarantola, A. (1984). Inversion of seismic reflection data in the acoustic approximation. *Geophysics*, 49(8):1259–1266.

Tarantola, A. (1988). Theoretical background for the inversion of seismic waveforms including elasticity and attenuation. *Pure and Applied Geophysics*, 128(1-2):365–399.

Tran, K., McVay, M., Faraone, M., and Horhota, D. (2013). Sinkhole detection using 2D full seismic waveform tomography. *Geophysics*, 78(5):R175–R183.

Trinh, P.-T., Brossier, R., Métivier, L., Tavard, L., and Virieux, J. (2018). Efficient time-domain 3D elastic and viscoelastic full-waveform inversion using a spectral-element method on flexible cartesian-based mesh. *Geophysics*, 84(1):R61–R83.

Virieux, J. and Operto, S. (2009). An overview of full-waveform inversion in exploration geophysics. *Geophysics*, 74(6):WCC1–WCC26.

Wittkamp, F., Athanasopoulos, N., and Bohlen, T. (2019). Individual and joint 2-D elastic full-waveform inversion of Rayleigh and Love waves. *Geophysical Journal International*, 216(1):350–364.

Xia, J., Miller, R., and Park, C. (1999). Estimation of near-surface shear-wave velocity by inversion of Rayleigh wave. *Geophysics*, 64(4):691–700.

Xia, J., Miller, R. D., Park, C. B., and Tian, G. (2002). Determining Q of near-surface materials from Rayleigh waves. *Journal of Applied Geophysics*, 51(2):121 – 129.

Xia, J., Xu, Y., Miller, R. D., and Ivanov, J. (2012). Estimation of near-surface quality factors by constrained inversion of Rayleigh-wave attenuation coefficients. *Journal of Applied Geophysics*, 82:137 – 144.

Yang, P., Brossier, R., Métivier, L., and Virieux, J. (2016). A review on the systematic formulation of 3-D multiparameter full waveform inversion in viscoelastic medium. *Geophysical Journal International*, 207(1):129–149.

Yang, P., Brossier, R., Métivier, L., Virieux, J., and Zhou, W. (2018). A time-domain preconditioned truncated Newton approach to visco-acoustic multiparameter full waveform inversion. *SIAM Journal on Scientific Computing*, 40(4):B1101–B1130.